

Empowering Low-Cost CMOS Cameras by Image Processing to Reach Comparable Results with Costly CCDs

Gözen Köklü · Julien Ghaye ·
Ralph Etienne-Cummings · Yusuf Leblebici ·
Giovanni De Micheli · Sandro Carrara

Published online: 20 September 2013
© Springer Science+Business Media New York 2013

Abstract Despite the huge research effort to improve the performance of the complementary metal oxide semiconductor (CMOS) image sensors, charge-coupled devices (CCDs) still dominate the cell biology-related conventional fluorescence microscopic imaging market where low or ultra-low noise imaging is required. A detailed comparison of the sensor specifications and performance is usually not provided by the manufacturers which leads the end users not to go out of the habitude and choose a CCD camera instead of a CMOS one. However, depending on the application, CMOS cameras, when empowered by image processing algorithms, can become cost-efficient solutions for conventional fluorescence microscopy. In this paper, we introduce an application-based comparative study between the default CCD camera of an inverted microscope (Nikon Ti-S Eclipse) and a custom-designed CMOS camera and apply efficient image processing algorithms to improve the performance of CMOS cameras. Quantum micro-bead samples (emitting fluorescence light at different intensity levels), breast cancer diagnostic tissue cell samples, and Caco-2 cell samples are imaged by both CMOS and CCD cameras. The results are provided to show the reliability of CMOS camera processed images and finally to be of assistance when scientists select their cameras for desired applications.

Keywords Fluorescence microscopy cameras · CMOS camera · CCD camera · CCD vs CMOS · CMOS image sensor · CCD image sensor

1 Introduction

Historically, charge-coupled devices (CCDs) have dominated the imaging sensor market. Today, the market share for complementary metal oxide semiconductor (CMOS) image sensors is increasing and even surpassing CCDs in terms of volume [1]. However, CCDs are still the dominating technology for high-quality imaging market and are used for high-cost imaging applications such as microscopy for life and material science applications in both clinical and educational domains. In the literature, there are many examples on the use of CCD cameras for detecting fluorescent labeled deoxyribonucleic acid (DNAs) or some expressions on the stained, fixed, or live cells. Some examples to that is imaging of growing DNA chains [2]; real-time detection of DNA hybridization to DNA microarrays [3]; monitoring of anticancer effects of some specific agents [4]; examining of cell polarity on stained, fixed, and live cells [5]; and obtaining quantitative information about the chromatin–DNA distribution inside the nucleus [6–8].

On the other hand, CMOS image sensors were mostly used in low-performance devices (e.g., toys, cell phones [9, 10]) due to their inherent advantages such as low power consumption, low cost, compactness, and high integration. Recently, this traditional misconception started to dissolve, and CMOS imagers started to show up in both high quality digital single-lens reflex (DSLR) cameras and biological applications. A couple of examples of CMOS cameras in biological applications include miniaturized fluorescence cameras for brain imaging [11–13] and fluorescence

G. Köklü (✉) · J. Ghaye · G. De Micheli · S. Carrara
Integrated Systems Laboratory (LSI), Swiss Federal Institute
of Technology, Lausanne, Switzerland
e-mail: gozen.koklu@epfl.ch

G. Köklü · Y. Leblebici
Microelectronic Systems Laboratory (LSM), Swiss Federal
Institute of Technology, Lausanne, Switzerland

R. Etienne-Cummings
Computational Sensory-Motor Systems Lab, Johns Hopkins
University, Baltimore, MD, USA

lifetime imaging with CMOS single-photon avalanche diodes (SPADs) [14, 15] where CMOS sensor speed advantage becomes crucial. However, the use of CMOS-based cameras in microscopy is still very limited, although a CMOS imager can perform as well as a CCD imager on various grounds, depending on the application specifications while usually costing less than CCDs. To do that, it is of great importance to mitigate the downside of CMOS sensors, especially higher noise, with image processing algorithms dedicated for quantitative fluorescence microscopy measurements [16, 17] and benefit from synthetic image generation techniques [18], to facilitate the progress on this domain.

In this paper, we target fluorescent detection systems in upright or inverted microscopes due to their popularity in cell-level biology and biochemistry for a variety of experimental, analytical, and quality control applications as described earlier. With the comparative study described in the following sections, we show that even a mid-performance CMOS camera when empowered by image processing algorithms can reach similar results with a widely used high-cost CCD camera results. This paper intends to show the potential use of CMOS cameras for microscopic applications, suggests to scientists to further diagnose their camera options before buying cameras, and proposes different image processing methods that can be applied to reduce different types of noise as well as to make an easy comparative study.

The structure of this paper is as follows: in Section 2, we describe the materials used in this experiment—the custom-designed CMOS camera, commercially available Nikon CCD camera and image intensity calibration kits. In Section 3, we present the methods that are used in this experiment: image processing algorithms including noise reduction algorithms, auto-thresholding, and image registration and resizing, and the use of image intensity calibration kits to calculate the relative intensities of each kit sample from the collected camera images. In Section 4, the results are presented based on the calculation of the relative intensities as well as the detection of the morphological patterns on the tissue samples for cancer diagnostics and Caco-2 cell lines by both cameras.

2 Materials

2.1 Custom-Designed CMOS Camera vs Default CCD Camera

In order to show the possible use of CMOS cameras for cell-level biological applications, we perform an application-based comparative study based on fluorescence imaging between the images collected from the default CCD camera of the Nikon Eclipse Ti (Nikon Instruments, Inc. Melville,

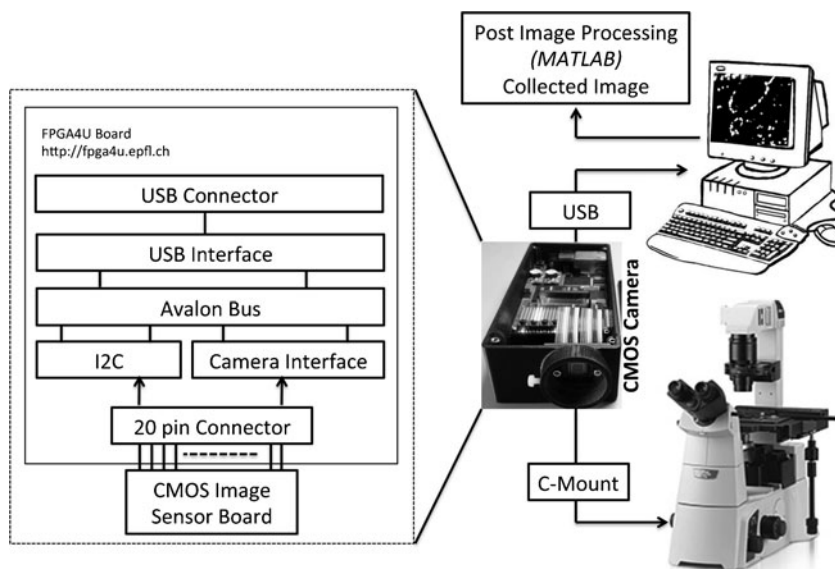
NY) inverted microscope and the custom-designed CMOS camera. The chosen CCD camera has been widely sold by Nikon for conventional microscopy applications, and the custom-designed CMOS camera is assembled by using a mid-performance CMOS imager. Since the focus of this paper is to introduce a low-cost replacement of standard CCD cameras, scientific CMOS (sCMOS) cameras, which are the high-cost, new-generation CMOS cameras providing a comparable and even better performance than electron multiplying charge-coupled devices (EMCCDs), are excluded from this study, and instead the standard CMOS camera images are empowered by image processing algorithms.

Figure 1 represents a block diagram of the entire fluorescence imaging system with the custom-designed CMOS camera from image collection to field programmable gate array (FPGA) interface. The more detailed picture of the custom-designed CMOS camera is shown in Fig. 2 where the CMOS image sensor and the FPGA4U [19] board are visible. The custom-designed CMOS camera replaces the CCD camera system which includes the CCD camera control unit and the CCD camera itself in two separate cases, where the imager inside the camera is Sony-ICX274AL [20]. The case for the camera has two openings from the back and the front, where the former is for the USB connector, and the latter is for interfacing output optics of the microscope using a C-mount system. The screw on the left side of the C-mount system is used to adjust coarsely the depth of focus. Although it is now possible to find CMOS cameras for microscopic applications in the market, at the time of setting up this system, due to the lack of available CMOS cameras for microscopy, we have chosen to build a custom-designed CMOS camera.

As seen in Fig. 1, the camera system includes an FPGA4U board and a printed circuit board (PCB) specifically built for the CMOS image sensor (Micron-MT9V032 [21]). The FPGA4U board includes a USB interface which allows to connect the board to a computer in order to both program the CMOS sensor and transfer the collected images. The collected images are later post-processed by using MATLAB software on the computer. The image sensor in the camera is a mid-performance black and white CMOS imager with 752×480 active pixels and 10-bit analog-to-digital converter (ADC) resolution. The sensor is connected to the FPGA board through the 20-pin connector which carries the inter-integrated circuit I^2C bus and the camera control signals. The I^2C interface is used to configure the internal registers of the sensor and more specifically the exposure time and analog gain for this application, and the Altera Design Software is used to write the VHDL code for camera control and synchronization units and to test them.

A more detailed comparison of the CMOS and CCD camera used in this experiment is shown in Table 1.

Fig. 1 System-level representation of image collection by CMOS camera



The costs of the two cameras given in Table 1 are estimated costs where the CCD camera cost is based on the information in [22] which is an Infinity X-32M camera that includes the same sensor as the Nikon CCD camera, and the CMOS camera cost is based on the Infinity 1-1M CMOS camera [23] which has similar characteristics as the custom-designed CMOS camera. The CMOS camera system not only allows a low-cost replacement of the CCD camera but also provides a highly flexible and reprogrammable camera unit. It also supports the implementation of additional functionalities and possibly image processing algorithms directly and rapidly on board.

Based on the sensor and camera data sheets, the comparison of the CMOS and CCD cameras used in this experiment is limited to Table 1. For the CCD camera, since the sensor and camera characteristics vary a lot, the information given on the data sheet of Infinity X-32M camera is more useful than that in the image sensor data sheet, but still limited. That is basically because a CCD imager outputs an analog

output and consists of pixel array and analog signal chain, while a CMOS image sensor consists of pixel array, analog signal chain, on-chip noise reduction, and digital readout providing a digital output as simply described in Fig. 3 [24]. Thus, the CCD sensor requires extra circuits for noise reduction as well as for digital readout (ADC), while a CMOS image sensor generates directly the digital output. The ADC resolution of the CMOS sensor used in this experiment is 10 bits, while the extra digital readout circuit combined with the CCD sensor generates 12 bits. For the consistency of the results in this paper, the images collected by the CCD camera is also converted to 10 bits by post-processing. However, it should be noted that it is possible to find in the market CMOS sensors also with 12-bit digital resolution and even higher [25, 26]. The most important parameters that would have a direct impact on the quality of the collected images are the *quantum efficiency and readout noise*. The readout noise can further be decreased by post-processing which will be explained in the upcoming sections; however, the quantum efficiency (QE) which refers to the fraction of photons incident on the detector surface that generate electrons plays a very important role in the detection limit of the two sensors. As seen in Table 1, the CCD camera has 1.22 times larger QE than the CMOS sensor. However, depending on the application or the light level, a lower quantum efficiency can also be enough to generate sufficient number of electrons or for more demanding applications possible to chose CMOS image sensors with higher QEs, i.e., 77 % at 515 nm [26].

To sum up, the comparison made on the sensor performances based on the *sensor* data sheets does not provide enough information to draw a conclusion to define the cameras' noise floor or minimum light detection limit or their performances for a specific application. The



Fig. 2 Custom-designed CMOS camera

Table 1 Comparison of CMOS and CCD cameras used in this experiment

	Nikon CCD camera [22]	CD CMOS [21]
Sensor	Sony ICX274AL [20]	MT9V032 [21]
Optical format (in)	1/1.8	1/3
Pixel size ($\mu\text{m} \times \mu\text{m}$)	4.40×4.40	6.0×6.0
Sensor area ($H \times V$)(mm^2)	57.8	12.99
Number of pixels ($H \times V$)	$1,628 \times 1,236$	752×480
Dynamic range (dB)	56	55
Quantum efficiency (QE) at 515 nm (%)	54	44
Pixel read noise (e^-)	12	25
Digital output (bits)	8/12	10
Price (Euros)	6,300	$\simeq 1,600$ [23]

performances given in the *camera* data sheets suffer from the same problem as well because of using different terms for the same performance parameters or by not specifying the measurement conditions clearly. Thus, the only comparable information we could achieve from the sensor and camera data sheets are limited to Table 1. However, the methods presented below can compare the two cameras based on the application-specific collected images which are the images of the artificial and real fluorescent samples. This work mainly compares a widely available high-cost CCD camera for microscopy use with a mid-performance low-cost CMOS camera. Obviously, the characteristics of the CMOS sensor can highly be improved by use of better-performing sensors from the market [25, 26] or from the literature [27, 28]. For other applications, the same metrics and post-processing algorithms or similar metrics can be used for comparison.

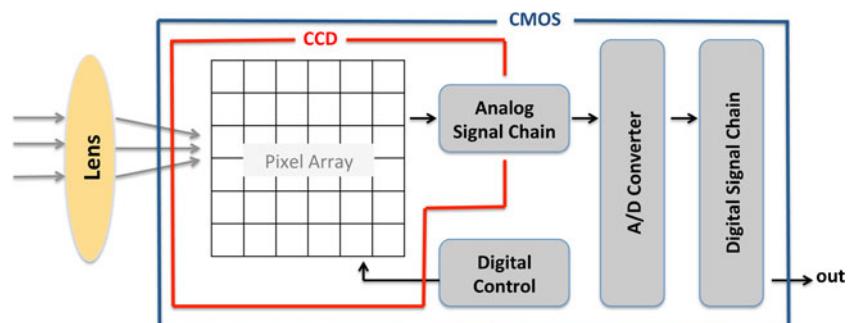
2.2 Image Intensity Calibration Kit

A microscope image intensity calibration kit is used to compare the quality of each camera. This kit provides fluorescent microspheres with fluorescence intensities ranging

from very low intensities, similar to the ones emitted by biological samples, to the brightest signal expected in most microscopy applications. The green calibration kit references as Invitrogen's InSpeck Green (505/515) Microscope Image Intensity Calibration Kit (Life Technologies Incorporation, Carlsbad, CA) used for this application which has excitation/emission wavelengths of 505/515 nm, and the diameter of each microsphere is 6 μm . According to the data sheet of the calibration kit, the kit includes five different samples of microspheres at relative intensities of 100, 30, 10, 3, 1, and 0.3 % which were determined using a Becton Dickinson FACScanTM flow cytometer. However, as listed in the data sheet, the actual relative fluorescence intensities of these components may vary somewhat from the values listed, depending on the kit and the production lot.

3 Methods

In order to provide a cost-efficient solution to high-cost CCDs, standard CMOS camera images are empowered with different image processing algorithms. First of all, fixed pattern noise (FPN) and temporal noise reduction algorithms are used. Later, we apply thresholding algorithms on CMOS and CCD camera images to extract the morphological patterns on the collected images and to create a comparison metric. In addition, we apply image registration and image resizing algorithms on the images collected by the CCD camera to keep the same area of interest with the images collected by the CMOS camera, and we finally compare the camera images from the calculated correlation value. First, we image fluorescence micro-bead samples (size of 6 μm) obtained from the microscope intensity calibration kit which emits light at 515 nm with different relative intensities (RIs) as 100, 33, 10, 3, 1, and 0.3 %. We calculate the RIs of these micro-bead samples by using a new metric called intensity per white pixel (I/WP) and compare the calculated RIs with both cameras. Second, we use a tissue sample obtained from breast cancer patients where an estrogen receptor (ER) expression emits low-intensity fluorescence light at 665 nm. More details on the tissue sample imaging can be found

Fig. 3 General view of CMOS and CCD cameras [24]

in [29]. Finally, we also applied the methods on images of fluorescent groups of Caco-2 cells. Using immunofluorescence techniques, we stained the naturally present glyceraldehyde 3-phosphate dehydrogenase (GAPDH) enzyme that we use as an example of nanometer-scale target by using a Texas Red compatible dye.

3.1 Image Processing Algorithms Applied on the CMOS Camera Images

3.1.1 Noise Removal

The goal of this research is to deal with low-light-emitting samples and applications. This is why noise contributors should be dealt with by reducing their impact on the useful signals. CMOS imagers are known to suffer from various noise sources which can be classified either as temporal noise or FPN [30]. Temporal noise (e.g., photon shot noise, readout noise) results from a stochastic process and cannot be fully determined nor mitigated for every pixel. However, the FPN is not a function of time and can be determined. It forms a constant pattern among the pixels/columns of the imager sensor. This problem arises from small differences in the individual responsivity of the pixels or the column amplifiers that are mostly caused by inhomogeneity in the manufacturing process. The noise removal algorithms are depicted in Section 4.

Fixed Pattern and Temporal Noise Reduction The FPN is generally divided into two components: dark signal nonuniformity (DSNU) and pixel response nonuniformity (PRNU). DSNU is an offset between pixels in dark without illumination (dark current generation variability), and PRNU is seen as a responsivity variation among pixels under illumination. Both of these noise sources are affected by the exposure time, the imager temperature, and the imager analog gain. When the light intensity received by the CMOS sensor through the fluorescence microscope is weak, it is required to program the CMOS image sensor at high exposure time and analog gain. This causes a huge FPN to appear, and a classic method to mitigate part of the DSNU is applied [31] on the CMOS images. First of all, a master dark frame (MDF) is generated by computing the median or the average frame out of a set of N dark frames. Second, the MDF is subtracted from any regular captured bright frame (i.e., containing the signal) at the same exposure and gain as the MDF. The de-noised frames are computed using the following:

$$F_{\text{corrected}} = \max(0, F_{\text{raw}} - \text{MDF}). \tag{1}$$

The sensor temperature should be stable during the calibration process, which can be achieved by letting the system on for a few minutes before capturing the dark frames.

On the other side, temporal noise is a function of time and includes different noise sources such as photon shot noise and readout noise. By collecting multiple images and averaging the collected images, temporal noise has been reduced.

Removal of Hot Spots/Pixels and Dead Pixels In every CMOS and CCD camera, there are dead and hot pixels. The amount of these defective pixels depends on temperature, technology, design, layout or micro-lenses. They may also appear due to aging of the sensor. Hot pixels generate higher leakage or dark current than normal. When an image is taken under long exposure time, longer than causing the pixel exceeding its linear charge capacity, they appear as bright spots and cause *salt and pepper* type of noise on the image. This type of noise cannot be removed by MDF generation and subtraction, since it is only visible at high exposure time. On the other hand, dead pixels are unresponsive stuck pixels, and no matter what the light intensity or exposure time, they do not respond to light. A common method to remove hot pixels or dead pixels is replacing them by the median value of the surrounding pixels. This remapping operation can be done by MATLAB median filtering—*medfilt2* operand or by an outlier removal algorithm. For this experiment, the following outlier removal algorithm has been used:

$$\Delta = (|I_{ij} - m|) \tag{2}$$

$$\forall i \in [1, v], \forall j \in [1, h] : I_{i,j} = \begin{cases} m & \text{if } \Delta > \text{Th,} \\ I_{ij} & \text{else.} \end{cases} \tag{3}$$

- I : intensity value of a pixel
- h : number of pixels at the horizontal direction
- v : number of pixels at the vertical direction
- m : Median value of the intensity values of pixels in a certain *window* of size (*radius* × *radius*) around the chosen pixel I_{ij}

If the Δ value is above a defined threshold (Th), the intensity value of the chosen pixel (I_{ij}) is replaced by the calculated median (m), and else, if the Δ is below the Th, no change is done and the pixel value is kept as it is. This method can be applied for both hot and dead pixels. Hot pixels are the pixels that exceed the level of the brightest neighboring pixel by more than the Th, and the dead pixels are the pixels that are darker than the darkest neighboring pixel by more than the Th. In both cases, they are replaced by the median of the surrounding pixels.

3.1.2 Auto-Thresholding

Thresholding method aims at selecting a threshold by maximizing a criterion measure that evaluates the “goodness”

of that threshold. For the experiments that are stated in this paper, the automatic thresholding method introduced by Otsu [32] is applied on the images by using MATLAB's *graythresh* function.

During the thresholding process, individual pixels in an image with an intensity value larger than a defined threshold value are converted to 1 ("object" pixels) where all the other pixel values below this threshold are converted to 0 ("background" pixels). Otsu's thresholding is a nonparametric method automatically selecting a threshold level for a gray-level image based on its histogram. The algorithm considers the image to be thresholded consisting of two classes of pixels as foreground and background and tries to achieve a thresholding value which minimizes the intra-class variation while at the same time allowing the maximization of the interclass variation.

The only input of the method is the normalized gray-level histogram of the image, which can also be seen as a probability distribution. Given a threshold value, the L bins of the histogram can be dichotomized in two classes: C_0 gathering the bins indexed by $[0, \dots, k - 1]$ and C_1 gathering the bins indexed by $[k, \dots, L - 1]$. The gray level corresponding to the bin k corresponds to the selected threshold.

Finding the optimal threshold k^* is reduced to solving

$$\max_{S^*} \left(\sigma_B^2(k) \right) \quad (4)$$

where S^* is the range of k over which the maximum is sought

$$S^* = \{k; \omega_0\omega_1 > 0, \text{ or } 0 < \omega_0 < 1\} \quad (5)$$

and σ_B^2 is referred to as the between-class variance defined by

$$\sigma_B^2 = \omega_0\omega_1(\mu_1 - \mu_0)^2 \quad (6)$$

for which ω_0 and ω_1 are the probability of class occurrences, and μ_0 and μ_1 are the class mean levels.

3.1.3 Image Registration

When the camera sensors have different pixel and pixel array sizes, image registration algorithms should be applied on the collected images to reach a fair comparison. Image registration is the process of aligning the pixels of two or more images of the same scene when one image is considered as a reference. In this experiment, the image registration algorithms basically include rotation, cropping, and scaling of the CCD camera images according to the CMOS camera images since the CCD array size is larger than the CMOS one. Below are the steps used for the registration of the CCD camera images until the highest correlation with the CMOS camera image is achieved:

1. Rotation of the image to solve the low or high angles of tilt issues that may appear when mounting the cameras (with MATLAB's *imrotate* function).
2. Cropping of the CCD camera image to reach same area of interest with the CMOS camera image. In this experiment, MATLAB's *imcrop* function is used to crop the CCD camera image of $1,628 \times 1,236$ according to the field of view of the CMOS camera image and finally an image with an array size of 989×631 is reached.
3. Resizing/scaling of the CCD camera image. The scaling factor for horizontal and vertical directions should be calculated separately depending on the size of each of the camera pixel. In this experiment, both of the camera pixels are in square which results in the same horizontal and vertical scaling factors. The scaling factor is calculated by dividing the CMOS pixel size to the CCD pixel size which is 1.3159 ($\text{CMOS pixel size}/\text{CCD pixel size} = 5.79\mu\text{m}/4.4\mu\text{m} = 1.3159$). By using the scaling factor, the cropped CCD image of 989×631 is resized to an image with an array size of 752×480 .

3.2 Calculation of the Relative Intensities from the Calibration Kit Samples

For measuring the microsphere RIs, we mount each microsphere sample of $5 \mu\text{L}$ on a separate glass slide. After letting each droplet dry on the glass slide, we imaged the samples with both CCD and CMOS cameras at different neutral density (ND) filter values where an ideal ND filter modifies the intensity of light equally according to its value. The collected images are later used to calculate the relative intensity values at the correct ND level as a comparison method. However, it is not straightforward to calculate the relative intensities of each sample since the number of microspheres per droplet is not known, and their distribution on the glass slide is not uniform which causes a varying number of microspheres for each sample and for each frame. This is why a metric called intensity per white pixel (I/WP) has been developed by using the calculated parameters total intensity (TI) and white pixel (WP). It is important to pay attention to the different pixel array size of CMOS and CCD sensors when annotating these parameter values. The CMOS sensor has 752×480 pixels, while the CCD sensor has $1,628 \times 1,236$. Ideally, this would result in 5.57 times larger TI and WP in CCD images than the CMOS ones if the responsivity and noise level of two sensors were the same, and microspheres have been uniformly distributed. However, none of these conditions are valid, and the number of microspheres per image and its ratio to the dark areas somehow differ from an ideal distribution. Thus, it is expected to achieve larger values of TI and WP for CCD images than for CMOS ones, but it is not possible to define the exact ratio of this increase. On the other hand, the I/WP and RI

parameters are independent of the area that is imaged or the pixel array size of the camera that is used, or the nonuniform distribution of the micro-beads. The immunity of these parameters to different conditions make these parameters reliable for this application, and they are also easily reusable for any camera comparison. The RI parameter calculated from the I/WP parameter is used as a comparison metric for this application since the micro-bead RI values are already known within a margin. Details of the calculations for each parameter is given below.

The TI parameter is the sum of each of the pixel intensity values on a gray-scale image and calculated as follows:

$$I_{\text{Total}} = \sum_{i=1}^v \sum_{j=1}^h I_{ij} \tag{7}$$

I : intensity value of a pixel

h : number of pixels at the horizontal direction

v : number of pixels at the vertical direction

The WP parameter is related with the *thresholding* concept which is explained earlier. By summing up the pixels above the threshold value, the total number of WP in an image can be calculated.

$$\forall i \in [1, v], \forall j \in [1, h] : BW_{i,j} = \begin{cases} 0 & \text{if } I_{ij} < V_{\text{Thresholding}} \\ 1 & \text{if } I_{ij} \geq V_{\text{Thresholding}} \end{cases} \tag{8}$$

where $V_{\text{Thresholding}}$ is the thresholding value calculated by MATLAB, and BW is the pixel value after thresholding, either black (0) or white (1).

$$BW_{\text{Total}} = \sum_{i=1}^v \sum_{j=1}^h BW_{ij} \tag{9}$$

By dividing the TI in a gray-scale image to the total number of WPs, the I/WP parameter is defined.

$$I/WP = \frac{I_{\text{Total}}}{BW_{\text{Total}}} \tag{10}$$

In order to improve the reliability of the RI results, the I/WP parameter is averaged over 20 images of the same sample which can be depicted as μ_N . The RI value among different samples can be formulated by the equation below where X represents the imaged sample of which the RI is being calculated.

$$RI = \frac{\sum_{N=1}^{20} \mu_N(\text{Sample}\%X)}{\sum_{N=1}^{20} \mu_N(\text{Sample}\%100)} \tag{11}$$

4 Results and Discussion

4.1 Comparison on Relative Intensity

In Tables 2 and 3, the sum of intensities of gray-scale images TI, sum of number of white pixels after thresholding WP, and intensity over white pixel I/WP results are shown for the micro-beads with 10 % of relative intensity with different ND values. In Fig. 4, the sum of intensity values in Tables 2 and 3 are graphically represented, and it is seen that for ND values from 1 to 4, the pixels are saturated, and from 128 to 1,024, they are under-illuminated. ND values from 8 to 64 represent an area of interest where WP count is almost constant as expected among light power. The WP parameter can also be used to define the exact illumination level. When decreasing the illumination level from the highest to the lowest by using the ND filters (changed from 1 to 1,024), it is found that the WP first starts decreasing due to the decrease in the number of saturated pixels, and after some point, this value start re-increasing due to the noise falling into the threshold level. When noise falls into the threshold level, the noise is also counted as part of the morphological pattern, and the black and white image is no longer correct. This is why the ND value corresponding to the lowest WP is considered as the correct illumination level for the sake of this measurement and are italicized in Tables 2 and 3. This behavior could be observed in all samples at different RIs, although in here, it is shown only for fluorescence micro-beads with illumination levels of 10 %.

The TI and WP parameters for CMOS and CCD images largely differ due to the large array size of the CCD sensor, the nonuniform distribution of the micro-beads, the unknown ratio between white and black pixels, and the difference in performance parameters of the two sensors. The WP parameter is less immune to the difference in the performance parameters but still immune to nonuniformity and

Table 2 Relative intensity calculations from CMOS camera images of microsphere slot of relative intensity 10 %

ND	$\sum(\text{intensity})$	$\sum(\text{white pixel})$	$TI/WP \times ND$
1,024	1,253	115,229	11.1370
512	1,279	116,210	5.6347
256	1,437	122,685	2.9993
128	1,739	19,519	11.9592
64	2,219	11,096	12.7979
32	3,514	11,201	10.0401
<i>16</i>	<i>5,483</i>	<i>11,158</i>	<i>7.8616</i>
8	9,808	11,236	6.9832
4	15,826	12,312	5.1418
2	20,996	14,812	2.8349
1	30,328	19,845	1.5282

Table 3 Relative intensity calculations from CCD camera images of microsphere slot of relative intensity 10 %

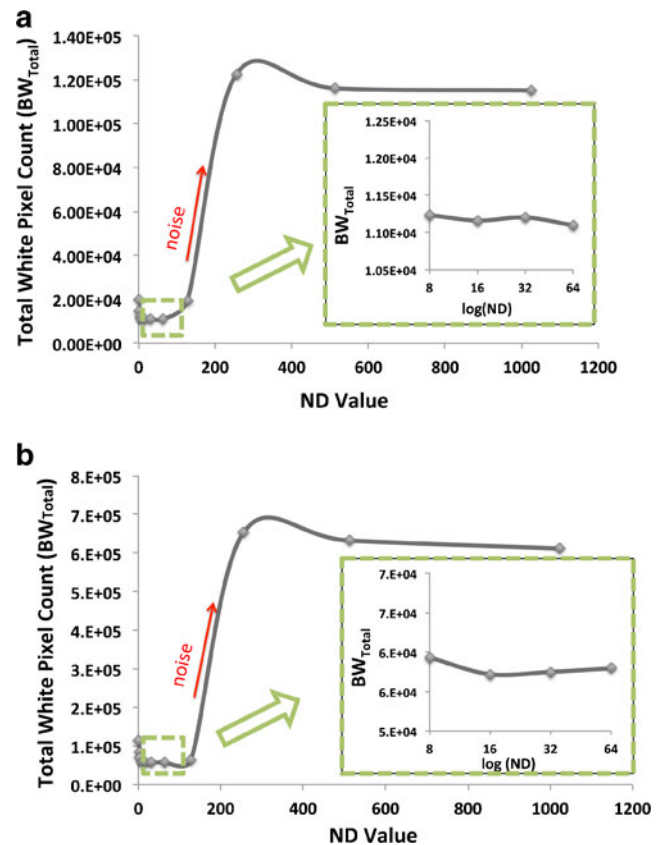
CMOS ND	CCD $\Sigma(\text{intensity})$	$\Sigma(\text{white pixel})$	TI/WP \times ND
1,024	12,404	611,848	20.7872
512	12,971	632,442	10.4196
256	14,127	653,572	5.5296
128	16,759	62,725	34.2016
64	20,852	57,960	23.0272
32	30,819	57,511	17.1488
<i>16</i>	<i>46,833</i>	<i>57,213</i>	<i>13.0976</i>
8	76,800	59,319	10.3576
4	101,165	68,321	5.9056
2	134,034	84,263	3.1814
1	195,104	114,228	1.7080

to the unknown ratio. The results of this parameter differ by a ratio of 5.2 for the two cameras which is close to the ideal value (CCD array size/CMOS array size = 5.57). Thus, neither the TI nor the WP parameters can be used to calculate the RIs. As mentioned earlier, the I/WP parameter is a better comparison parameter since it is not dependent on the array size or the nonuniformity of micro-beads' distribution. The italicized values in Tables 2 and 3 show that the calculated I/WP for the CCD image is 13.09 and 7.86 for the CMOS camera image for the same illumination level. This value can be interpreted similar to the system gain (K) in the linear region of a sensor which is defined as digital number (DN)/ e^- . This commonly known system gain parameter defines the number of digital numbers per electron or vice versa, where in this method, the I/WP parameter defines the number of digital numbers per white pixel.

The RI parameter on the other side compares the two cameras in terms of their imaging capabilities, providing a relative value with respect to the highest intensity sample. Thus, we achieve a direct comparison of the sensor imaging capabilities for this light range. The calculation method for RIs and results are shown in the next section.

4.2 Comparison on Imaging

In Tables 4 and 5, the calculated RIs for both CMOS and CCD camera images are shown with the parameters that are used. The calculated results vary from the expected relative intensities for both CMOS and CCD camera images. The variation for CMOS images for all intensity levels in average is 28.6 %, while it is 30.4 % for the CCD images. This variation was expected, as stated from the data sheet of the fluorescence, due to the variation of the production lot and also due to the difference in the calculation technique. However, despite the variation of calculated RIs from the

**Fig. 4** Total white pixel variation of a thresholded image with respect to ND filter values. **a** Measured on images collected by CMOS camera, **b** Measured on images collected by CCD camera

expected values, the results are consistent for both CMOS and CCD camera images, and the variation among the two camera images is only 4.79 %. This means that both cameras are capable of generating similar quality images as well as close quantitative results from a large-scale intensity fluorescence samples.

In this section, the image processing algorithms explained in Section 3.1 are applied on the CMOS and/or CCD camera images step by step. First, due to the high exposure time in CMOS camera, FPN noise becomes critical, and FPN noise reduction algorithm is applied on both

Table 4 Calculated relative intensities of microspheres by CMOS camera

Expected RI (%)	μ_N	ND	$\mu_N \times ND$	Calculated RI (%)
100	0.4222	256	108.1	100
30	0.3559	128	45.55	42.15
10	0.4914	16	7.86	7.27
3	0.3458	8	2.77	2.56
1	0.5657	2	1.13	1.05
0.3	0.5072	1	0.51	0.47

Table 5 Calculated relative intensities of microspheres by CCD camera

Expected RI (%)	μ_N	ND	$\mu_N \times ND$	Calculated RI (%)
100	0.76	256	194.81	100
30	0.6053	128	77.48	39.77
10	0.82	16	13.10	6.72
3	0.6065	8	4.85	2.49
1	0.55	4	2.2	1.13
0.3	0.91	1	0.91	0.47

tissue and Caco-2 cells' CMOS camera images. Second, to remove both *hot* and *dead pixel* outliers which are numerically distant from the surrounding pixel values on the image, the outlier removal algorithm is applied on the CMOS and CCD camera images. Later, the auto-thresholding algorithm is used for both camera images for quantitative calculations and comparison as well as for better visibility of the morphological patterns expressed on the cells. Finally, the CCD camera images are registered and resized according to the CMOS camera images. With this method, the CCD images of 1,200 V \times 1,600 H are converted to images of 480 V \times 752 H. In order to keep the experimental setup the same for both cameras, the same light intensity (ND filter = 1) and microscope optics and objectives ($\times 40$, numerical aperture

= 0.75) are used for both camera image acquisitions. The light emitted from the ER expression in tissue cells and the GAPDH expression in Caco-2 cells are both much lower than the micro-beads even at the lowest intensities. That is why the samples have been imaged at very high exposure time (1s) and analog gain ($8\times/16\times$) for both camera experiments.

4.2.1 Tissue Sample Imaging

The sample is a breast cancer diagnostic sample that the nuclear ER expression emits fluorescence light at 665 nm. ER is detected by indirect immunohistochemical reaction [33, 34] by using monoclonal mouse antihuman anti-ER receptor antibody as primary antibody (clone 6F11, Leica Microsystems) and Alexa Fluor 647 conjugated goat anti-mouse polyclonal IgG antibody (Invitrogen) as secondary antibody.

First, from the CMOS camera raw images (Fig. 5a), the MDF (Fig. 5b) is subtracted, and the corrected image is obtained as seen in Fig. 5c. Contrast enhancement is applied on this image in order to increase the visibility of *hot pixels/spots*. Later, the outlier removal algorithm is applied on this image. Finally, the thresholding method is applied on the image which is shown in Fig. 5e which improves

Fig. 5 CMOS and CCD camera images of ER detection from tissue samples (Exposure = 1s, Gain = $8\times$) [29]. **a** CMOS gray-scale camera image before noise removal (with DSNU), **b** CMOS camera master dark frame (MDF), **c** CMOS gray-scale camera image after FPN removal (without DSNU) (Contrast enhancement for better display of salt and pepper noise caused by hot pixels), **d** CCD camera gray-scale image (Enhanced contrast), **e** CMOS camera B/W image after Otsu's auto-thresholding method, **f** CCD camera BW image after Otsu's auto-thresholding method

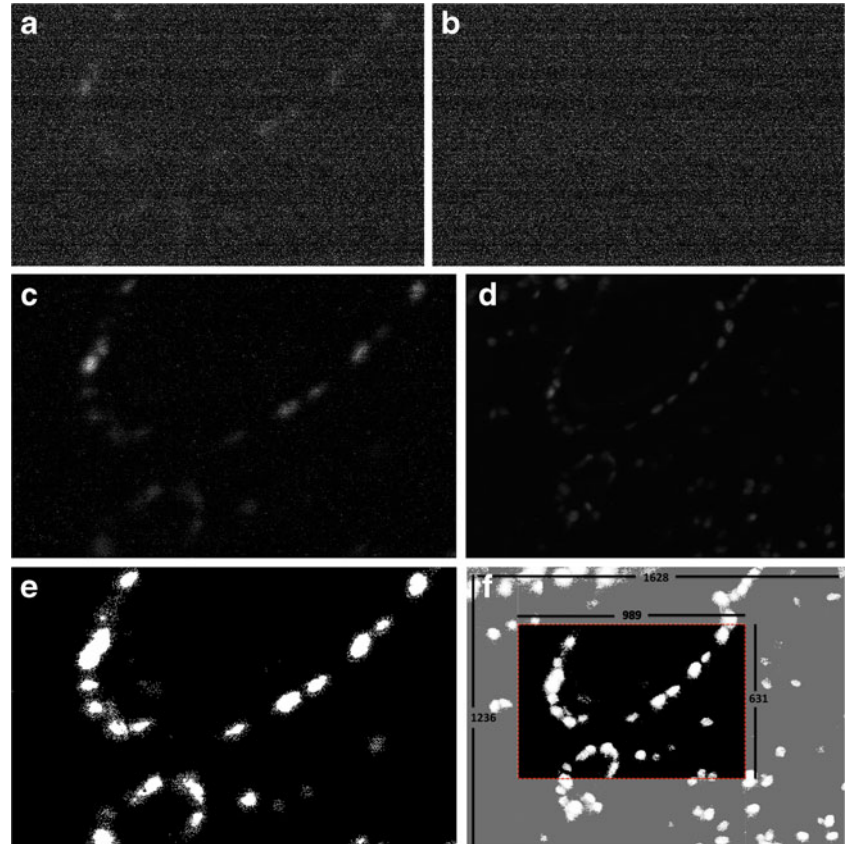
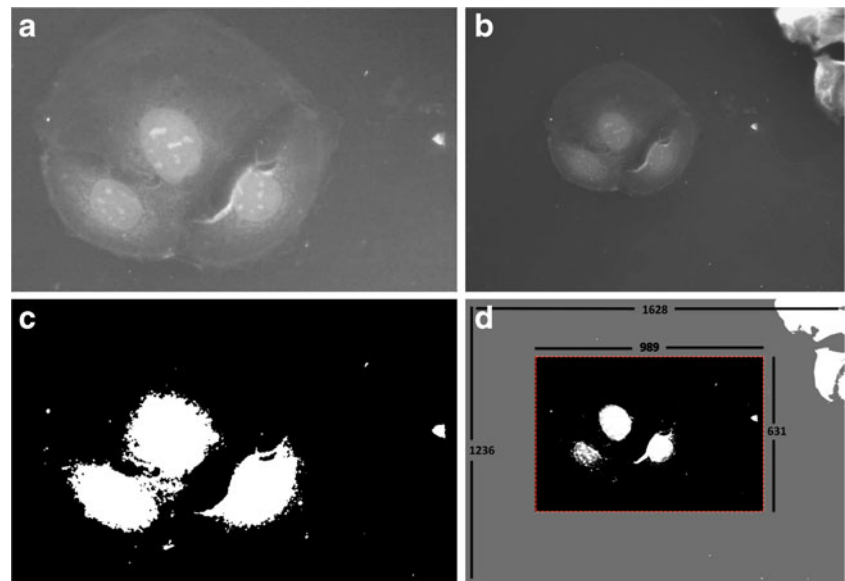


Fig. 6 CMOS and CCD camera images of GAPDH protein expression on Caco-2 cells (Exposure = 1s, Gain = 16 \times). **a** CMOS gray-scale camera image after FPN removal (without DSNU), **b** CCD gray-scale camera image, **c** CMOS black and white camera image after Otsu's auto-thresholding method, **d** CCD black and white camera image after Otsu's auto-thresholding method



the localization of the morphological pattern. For the CCD images seen in Fig. 5d, again the outlier removal algorithm is applied as well as the auto-thresholding method. The resulting image after auto-thresholding is seen in Fig. 5f.

4.2.2 GAPDH Gene Expression on Caco-2 Cells

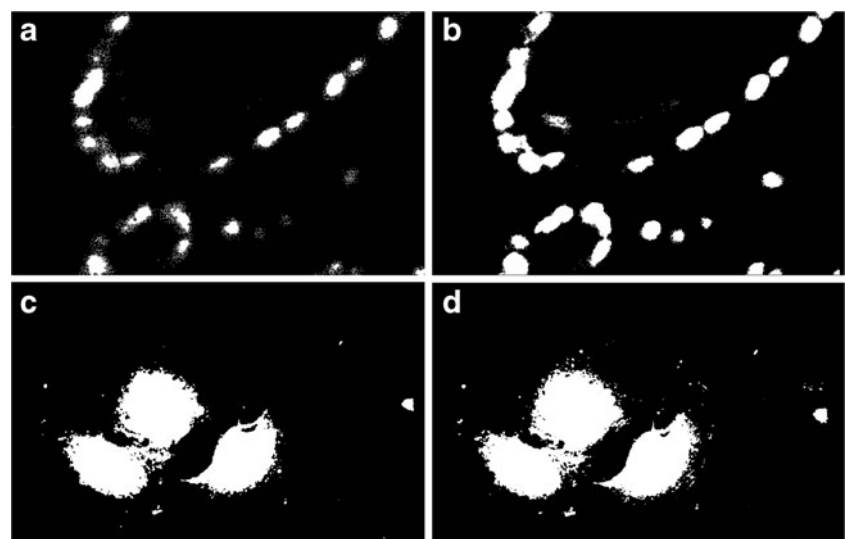
Human colon adenocarcinoma (Caco-2) cells are commonly used in pharmaceutical researches as an in vitro model of the human small intestinal mucosa in order to monitor the drug uptake and transport. Since the culturing of mature intestinal epithelial cells are very difficult, recently, Caco-2 cell lines have taken a lot of attention. In [35], Caco-2 cell monolayers have been proposed as a model for drug transport across the intestinal mucosa. In addition, in [36], induction of Toll-like receptor (TLR) proteins with lipopolysaccharides (LPS)

has been shown on Caco-2 cells to investigate the inflammation in the gastrointestinal tract (GIT) epithelial cells, and a nutrition platform mimicking the human GIT within the frame of these results have been proposed.

Due to the popularity of Caco-2 cells in pharmaceutical research and nutrition analysis on human health, we use a Caco-2 cell sample with Glyceraldehyde 3-phosphate dehydrogenase (GAPDH) expression to show the possible use of CMOS cameras on nanometer-scale applications. Using immunofluorescence techniques, the naturally present GAPDH enzyme is stained with a Texas-red compatible dye.

Similar to the tissue sample images, again, CMOS camera images are corrected with FPN removal algorithm and converted to black and white images with the auto-thresholding algorithm as seen in Fig. 6a, c. For the CCD

Fig. 7 CMOS and CCD camera image comparison. **a** Tissue sample image with CMOS camera, **b** Registered and resized CCD camera tissue sample image (752 \times 480), **c** Caco-2 cell line CMOS camera image, **d** registered and resized CCD camera Caco-2 cell line image (752 \times 480)



camera Caco-2 cell images, the same procedure as in the tissue sample imaging is applied, and results are shown in Fig. 6b, d. Three Caco-2 cells are visible in these images, and the GAPDH protein is expressed in the nucleus of the cells.

4.2.3 Comparison of CCD and CMOS Camera Images

Figure 7 helps to make a direct comparison on the CMOS and registered and resized CCD camera tissue and Caco-2 cell images.

In Fig. 7a, b, it is seen that both cameras are capable of detecting the morphological pattern of the ER receptor expression at the nucleus level that can be found in the breast tissue. The correlation coefficient calculated among these two images by using the MATLAB cross-correlation function of *corr2* is found to be 0.65.

In Fig. 7c, d, it is visibly possible to conclude that both cameras are capable of detecting the morphological pattern of the GAPDH protein expression at the Caco-2 cell nucleus level. A correlation value among these two black and white images is found as 0.84.

These high correlation values confirm the conclusion that was drawn earlier that the CMOS cameras when empowered with image processing algorithms should be considered for cellular-level optical studies.

5 Conclusion

In this paper, we proposed a comparative study between a CCD and a CMOS camera with respect to their performances for imaging on artificial fluorescence beads and a biological tissue sample by using optical microscopy. The calculations applied on the images of artificial fluorescence beads have shown that even a mid-performance, low-cost CMOS and a high-cost CCD cameras extract very close information where the final variation among the relative intensities is only 4.79 %. For the cancer diagnostic and Caco-2 samples, since ER and GAPDH expressions emit even lower fluorescence light than the micro-beads with the lowest intensities, the effect of the noise reduction algorithms have become even more crucial and visible. At this high exposure rates, although the initial CMOS image has been very noisy, after applying proper image processing algorithms, the CMOS camera was capable of generating the same morphological pattern as the CCD camera image. Therefore, this paper demonstrates that CMOS cameras are recommended for investigations of cells and tissues when dealing with fluorescence microscopy. It paves the way for biologists to further investigate their camera options as well as decrease their instrument costs. Undoubtedly, the trend towards using low-cost CMOS cameras is even more

important when standard microscopy is replaced by (possibly disposable) lab-on-chip platforms.

Acknowledgments The research work presented in this paper was funded by the NutriCHIP project with a grant from the Swiss Nano-Tera.ch initiative, evaluated by the Swiss National Science Foundation. It was also partially supported by the NanoSys project, in the program ERC-2009-AdG-246810. Finally, the authors would like to thank to Ata Tuna Çiftlik from LMIS2 (Microsystems Laboratory 2), EPFL, for their support in tissue sample preparation; and Ali Galip Bayrak from LAP (Processor Architecture Laboratory), EPFL, for his precious suggestions and the useful discussions.

References

1. Fossum, E.R., Hyneczek, J., Tower, J., Teranishi, N., Nakamura, J., Magnan, P., Theuwissen, A. (2009). Special issue on solid-state image sensors. *IEEE Transactions on Electron Devices*, 56(11), 2376–2379.
2. Ansoorge, W.J. (2009). Next-generation DNA sequencing techniques. *New Biotechnology*, 25(4), 195–203.
3. Sapuppo, F., Intaglietta, M., Bucolo, M. (2008). Bio-microfluidics real-time monitoring using CNN technology. *IEEE Transactions on Biomedical Circuits and Systems*, 2(2), 78–87.
4. Kang, H.W., Muramatsu, H., Lee, B.J., Kwon, Y.S. (2010). Monitoring of anticancer effect of cisplatin and 5-fluorouracil on HepG2 cells by quartz crystal microbalance and micro CCD camera. *Biosensors and Bioelectronics*, 26(4), 1576–1581.
5. Osmani, N., Peglion, F., Chavrier, P., Etienne-Manneville, S. (2010). Cdc42 localization and cell polarity depend on membrane traffic. *The Journal of Cell Biology*, 191(7), 1261–1269.
6. Nicolini, C., Carrara, S., Mascetti, G. (1997). High order DNA structure as inferred by optical fluorimetry and scanning calorimetry. *Molecular Biology Reports*, 24(4), 235–246.
7. Mascetti, G., Vergani, L., Diaspro, A., Carrara, S., Radicchi, G., Nicolini, C. (1998). Effect of fixatives on calf thymocytes chromatin as analyzed by 3D high-resolution fluorescence microscopy. *Cytometry*, 23(2), 110–119.
8. Mascetti, G., & Carrara, S. (2001). Relationship between chromatin compactness and dye uptake for in situ chromatin stained with DAPI. *Cytometry*, 44(2), 113–119.
9. Fossum, E.R. (1993). Active pixel sensors: are CCD's dinosaurs? In *Proceedings SPIE* (Vol. 1900, pp. 1–3).
10. Fossum, E.R. (1997). CMOS image sensors: electronic camera-on-chip. *IEEE Transactions Electron Devices*, 44, 1689–1698.
11. Murari, K., Etienne-Cummings, R., Cauwenberghs, G., Thakor, N. (2010). An integrated imaging microscope for untethered cortical imaging in freely-moving animals. In *Engineering in medicine and biology society (EMBC), 2010 annual international conference of the IEEE* (pp. 5795–5798).
12. Murari, K., Greenwald, E., Etienne-Cummings, R., Cauwenberghs, G., Thakor, N. (2009). Design and characterization of a miniaturized epi-illuminated microscope. In *Engineering in medicine and biology society, 2009. EMBC 2009. Annual international conference of the IEEE* (pp. 5369–5372).
13. Ghosh, K.K., Burns, L.D., Cocker, E.D., Nimmerjahn, A., Ziv, Y., El Gamal, A., Schnitzer, M.J. (2011). Miniaturized integration of a fluorescence microscope. *Nature Methods*, 8(10), 871–878.
14. Li, D.U., Arlt, J., Richardson, J., Walker, R., Buts, A., Stoppa, D., Henderson, R. (2010). Real-time fluorescence lifetime imaging system with a $32 \times 320.13\mu\text{m}$ CMOS low dark-count single-photon avalanche diode array. *Optics Express*, 18(10), 10257–10269.

15. Schwartz, D.E., Charbon, E., Shepard, K.L. (2008). A single-photon avalanche diode array for fluorescence lifetime imaging microscopy. *IEEE Journal of Solid-State Circuits*, 43(11), 2546–2557.
16. Mutch, S.A., et al. (2007). Deconvolving single-molecule intensity distributions for quantitative microscopy measurements. *Biophysical Journal*, 92.8, 2926–2943.
17. Cronin, B., de Wet, B., Wallace, M.I. (2009). Lucky imaging: improved localization accuracy for single molecule imaging. *Bio-physical Journal*, 96.7, 2912–2917.
18. Ghaye, J., De Micheli, G., Carrara, S. (2012). Simulated biological cells for receptor counting in fluorescence imaging. *Bio-NanoScience*, 2.2, 94–103.
19. Favi, C., Beuchat, R., Jimenez, X., Jenne, P. (2009). From gates to multi-processors learning systems hands-on with FPGA4U in a computer science programme. In *Proceedings of the 2009 workshop on embedded systems security (WESS)*. Grenoble.
20. PointGrey Research (2010). *Technical application note TAN2008006*, Richmond. http://www.ptgrey.com/support/downloads/documents/_TAN2008006_Sensor_Response_Curve_Comparison_for_ICX445.pdf. Accessed 2 Jul 2012.
21. Aptina Imaging Corporation (2006). *1/3-inch wide-VGA CMOS digital image sensor*, San Jose. http://www.aplina.com/products/image_sensors/mt9v032d00stm/. Accessed 2 Jul 2012.
22. Lumenera Corporation (2008). *Infinity X-32M, 32 megapixel CCD USB 2.0 camera*. <http://www.emsdiasum.com/microscopy/technical/datasheet/95116-95117.pdf>. Accessed 2 Jul 2012.
23. Lumenera Corporation (2010). *Infinity 1-1M, 1.3 megapixel monochrome camera*. <http://www.oem-optical.com/lumenera-cmos-1model.html>. Accessed 2 Jul 2012.
24. Theuwissen, A. (2012). Digital imaging: image capturing, image sensors—technologies and applications. In *Annual international courses in telecommunications semiconductor technology nanotechnology, CEI-Europe*. Barcelona.
25. Aptina Imaging Corporation (2012). *1/2.5-Inch 5MP CMOS digital image sensor*, San Jose. http://www.aplina.com/products/image_sensors/mt9p031i12stm/. Accessed 2 Jul 2012.
26. Aptina Imaging Corporation (2012). *1 Megapixel 1/3-inch digital image sensor Recon and iLCC*, San Jose. http://www.aplina.com/products/image_sensors/ar0130cs. Accessed 2 Jul 2012.
27. Johansson, R., Storm, A., Stephansen, C., Eikedal, S., Willassen, T., Skaug, S., Perks, D. (2011). A 1/13-inch 30fps VGA SoC CMOS image sensor with shared reset and transfer-gate pixel control. In *Solid-state circuits conference digest of technical papers (ISSCC), 2011 IEEE international* (pp. 414–415).
28. Seo, M.W., Suh, S.H., Iida, T., Takasawa, T., Isobe, K., Watanabe, T., Kawahito, S. (2012). A low-noise high intrasene dynamic range CMOS image sensor with a 13 to 19b variable-resolution column-parallel folding-integration/cyclic ADC. *IEEE Journal of Solid-State Circuits*, 47(1), 272–283.
29. Koklu, G., Ghaye, J., Beuchat, R., De Micheli, G., Leblebici, Y., Carrara, S. (2012). Quantitative comparison of commercial CCD and custom-designed CMOS camera for biological applications. In *2012 IEEE international symposium on circuits and systems (ISCAS)* (pp. 2063–2066).
30. Bigas, M., Cabruja, E., Forest, J., Salvi, J. (2006). Review of CMOS image sensors. *Microelectronics Journal*, 37(5), 433–451.
31. Schöberl, M., Senel, C., Fössel, S., Bloss, H., Kaup, A. (2009). Non-linear dark current fixed pattern noise compensation for variable frame rate moving picture cameras. In *Proceedings 17th European signal processing conference (EUSIPCO)* (pp. 268–272).
32. Otsu, N. (1975). A threshold selection method from gray-level histograms. *Automatica*, 11(285–296), 23–27.
33. Song, B., Sivagnanam, V., Vandevyver, C.D., Hemmila, I., Lehr, H.A., Gijs, M.A., Bünzli, J.C.G. (2009). Time-resolved lanthanide luminescence for lab-on-a-chip detection of biomarkers on cancerous tissues. *Analyst*, 134(10), 1991–1993.
34. Ciftlik, A.T., Song, B., Vandevyver, C., Bünzli, J.C., Lehr, H.A., Gijs, M. (2010). Fast immunohistochemical biomarker detection device for cancer tissue slices. In *Proceedings of 14th international conference on miniaturized systems for chemistry and life sciences (MicroTAS)* (pp. 699–70).
35. Hilgers, A.R., Conradi, R.A., Burton, P.S. (1990). Caco-2 cell monolayers as a model for drug transport across the intestinal mucosa. *Pharmaceutical Research*, 7.9, 902–910.
36. Vergeres, G., et al. (2012). The NutriChip project translating technology into nutritional knowledge. *British Journal of Nutrition*, 1.1, 1–7.